The Astrophysical Journal, 967:11 (11pp), 2024 May 20 https://doi.org/10.3847/1538-4357/ad33c9

TEMPLATES: Characterization of a Merger in the Dusty Lensing SPT0418–47 System

Jared Cathey[1], Anthony H. Gonzalez[1], Sidney Lower[1], Kedar A. Phadke[2,3], Justin Spilker[4], Manuel Aravena[5], Matthew Bayliss[6], Jack E. Birkin[4], Simon Birrer[7], Scott Chapman[8,9,10,11], Håkon Dahle[12], Christopher C. Hayward[13], Yashar Hezaveh[13,14,15,16], Ryley Hill[10], Taylor A. Hutchison[17,27], Keunho J. Kim[6], Guillaume Mahler[18,19], Daniel P. Marrone[20], Desika Narayanan[21], Alexander Navarre[6], Cassie Reuter[2], Jane R. Rigby[22], Keren Sharon[23], Manuel Solimano[24], Nikolaus Sulzenauer[25], Joaquin Vieira[2,3,26], and David Vizgan[2]

[1] Department of Astronomy, University of Florida, 211 Bryant Space Sciences Center, Gainesville, FL 32611, USA; jaredcathey@ufl.edu
[2] Department of Astronomy, University of Illinois, 1002 West Green St., Urbana, IL 61801, USA
[3] Center for AstroPhysical Surveys, National Center for Supercomputing Applications, 1205 West Clark Street, Urbana, IL 61801, USA
[4] Department of Physics and Astronomy and George P. and Cynthia Woods Mitchell Institute for Fundamental Physics and Astronomy, Texas A&M University, 4242 TAMU, College Station, TX 77843-4242, USA
[5] Núcleo de Astronomía, Facultad de Ingeniería y Ciencias, Universidad Diego Portales, Av. Ejercito 441, 8370191, Santiago, Chile
[6] Department of Physics, University of Cincinnati, Cincinnati, OH 45221, USA
[7] Department of Physics and Astronomy, Stony Brook University, Stony Brook, NY 11794, USA
[8] Department of Physics and Atmospheric Science, Dalhousie University, Halifax, NS, B3H 4R2, Canada
[9] NRC Herzberg Astronomy and Astrophysics, 5071 West Saanich Rd, Victoria, BC, V9E 2E7, Canada
[10] Department of Physics and Astronomy, University of British Columbia, Vancouver, BC, V6T 1Z1, Canada
[11] Eureka Scientific Inc, Oakland, CA 94602, USA
[12] Institute of Theoretical Astrophysics, University of Oslo, P.O. Box 1029, Blindern, NO-0315 Oslo, Norway
[13] Center for Computational Astrophysics, Flatiron Institute, 162 5th Ave., 10010, New York, NY, USA
[14] Department of Physics, Université de Montréal, Montréal, QC, H2V 0B3, Canada
[15] Ciela—Montreal Institute for Astrophysical Data Analysis and Machine Learning, Montréal, QC, H2V 0B3, Canada
[16] Mila—Quebec Artificial Intelligence Institute, Montréal, QC, H2V 0B3, Canada
[17] Observational Cosmology Lab, Code 665, NASA Goddard Space Flight Center, 8800 Greenbelt Rd, Greenbelt, MD 20771, USA
[18] Centre for Extragalactic Astronomy, Durham University, South Rd., Durham, DH1 3LE, UK
[19] Institute for Computational Cosmology, Durham University, South Rd., Durham, DH1 3LE, UK
[20] Steward Observatory, University of Arizona, 933 North Cherry Ave., Tucson, AZ 85721, USA
[21] Department of Astronomy, University of Florida, Gainesville, FL 32611-2055, USA
[22] Observational Cosmology Lab, Code 665, NASA Goddard Space Flight Center, Greenbelt, MD 20771, USA
[23] University of Michigan, Department of Astronomy, 1085 South University Ave., Ann Arbor, MI 48109, USA
[24] Instituto de Estudios Astrofísicos, Facultad de Ingeniería y Ciencias, Universidad Diego Portales, Avenida Ejército Libertador 441, 8370191, Santiago, Chile
[25] Max-Planck-Institut für Radioastronomie, Auf dem Hügel 69, 53121 Bonn, Germany
[26] Department of Physics, University of Illinois, 1110 West Green St., Urbana, IL 61801, USA
Received 2023 June 22; revised 2024 February 6; accepted 2024 February 16; published 2024 May 13

Abstract

We present JWST and Atacama Large Millimeter/submillimeter Array (ALMA) imaging for the lensing system SPT0418−47, which includes a strongly lensed, dusty, star-forming galaxy at redshift z = 4.225 and an associated multiply imaged companion. The JWST NIRCam and MIRI imaging observations presented in this paper were acquired as part of the Early Release Science program Targeting Extremely Magnified Panchromatic Lensed Arcs and Their Extended Star formation (TEMPLATES). This data set provides robust multiwavelength detections of stellar light in both the main (SPT0418A) and companion (SPT0418B) galaxies, while the ALMA detection of [C II] emission confirms that SPT0418B lies at the same redshift as SPT0418A. We infer that the projected physical separation of the two galaxies is 4.42 ± 0.05 kpc. We derive total magnifications of μ = 29 ± 1 and μ = 4.1 ± 0.7 for SPT0418A and SPT0418B, respectively. We use both PROSPECTOR and CIGALE to derive stellar masses. We find that SPT0418A has a stellar mass of $M_* = 3.4^{+1.1}_{-0.6} \times 10^{10} M_\odot$ from PROSPECTOR or $M_* = 1.5 \pm 0.3 \times 10^{10} M_\odot$ from CIGALE. The stellar mass ratio of SPT0418A and SPT0418B is roughly between 4 and 12 ($4.2^{+1.9}_{-1.6}$ for PROSPECTOR and 7.5 ± 3.7 for CIGALE). We see evidence of extended structure associated with SPT0418A that is suggestive of a tidal feature. These features, along with the close projected proximity, imply that the system is interacting. Interestingly, the star formation rates and stellar masses of both galaxies are consistent with the main sequence of star-forming galaxies at this epoch, indicating that this ongoing interaction has not noticeably elevated the star formation levels.

Unified Astronomy Thesaurus concepts: High-redshift galaxies (734); Strong gravitational lensing (1643); Galaxy mergers (608); Einstein rings (451)

1. Introduction

In the standard paradigm of galaxy formation, present-day spiral galaxies are products of hierarchical assembly, with the disks arising after the last major merger either as a byproduct of dissipative mergers (e.g., Robertson et al. 2006; Governato et al. 2009) or from subsequent gas accretion and minor

[27] NASA Postdoctoral Fellow.

dissipative mergers (e.g., Baugh et al. 1996; Steinmetz & Navarro 2002). In this picture, dynamically cold disks become increasingly rare at higher redshifts (e.g., Hopkins et al. 2010). Moreover, mergers can induce bursts of star formation, and hence can drive star formation at early times when mergers are expected to be more frequent (Sanders et al. 1988; Hopkins et al. 2008; Sotillo-Ramos et al. 2022). Studies of high-redshift, dusty, star-forming galaxies (DSFGs) have supported a picture in which many of these strongly star-forming galaxies are major mergers (Engel et al. 2010; Alaghband-Zadeh et al. 2012; Marrone et al. 2018; Litke et al. 2019; Perry et al. 2022). Theoretical works, such as those of Narayanan et al. (2015) and Hayward et al. (2011), have also investigated whether DSFGs are a homogeneous population and found that a significant fraction could be quiescent disks rather than late-stage major mergers.

A counterpoint to this picture was presented by Rizzo et al. (2020), who used the Atacama Large Millimeter/submillimeter Array (ALMA) to investigate the kinematics of the DSFG SPT0418−47 at $z = 4.225$. Rizzo et al. (2020) found that SPT0418−47 exhibits orderly disk rotation, with a ratio of rotational to turbulent velocity $V/\sigma = 9.7 \pm 0.4$ for the gas. This well-ordered rotation contrasts with the picture of clumpy, turbulent gas expected for such a young system (Pillepich et al. 2019). Rizzo et al. (2021) have reported high V/σ ratios for five additional DSFGs at similar redshift, raising the surprising possibility that disks are common in these systems and that the high star formation rates (SFRs) are driven by purely internal processes.

SPT0418−47, the galaxy studied by Rizzo et al. (2020), is one of four targets of the JWST Early Release Science (ERS) program Targeting Extremely Magnified Panchromatic Lensed Arcs and their Extended Star formation (TEMPLATES; ERS Program 1355; PI: J. R. Rigby; Co-PI: J. D. Vieira). The overall aim of TEMPLATES is to use multiple tracers to study the spatially resolved star formation in four strongly lensed galaxies spanning a range of redshift and SFRs. SPT0418−47 has the highest redshift of these four targets, at $z = 4.225$. The aim of this paper is to use the JWST imaging, augmented by new ALMA observations, to better elucidate the nature of SPT0418−47. We use NIRCam (Rieke et al. 2023) and MIRI (Wright et al. 2023) imaging to spatially resolve the stellar emission in this system. We combine JWST imaging and ALMA [C II] data and investigate the environment of this system to discern whether this system is isolated or is dynamically interacting. We also determine the stellar mass and specific star formation rate (sSFR) of the system to quantify the level at which its star formation is elevated relative to the star-forming main sequence. For this analysis, we employ spectral energy distribution (SED) modeling and use the source plane reconstruction for magnification correction.

Originally discovered as a submillimeter source by the South Pole Telescope (SPT; Vieira et al. 2013), SPT0418−47 is known to have a high SFR ($\sim 280\ M_\odot\ \mathrm{yr}^{-1}$) with a dense, solar-metallicity interstellar medium, from observations with the Atacama Pathfinder EXperiment and ALMA (De Breuck et al. 2019) and from JWST spectroscopy (Birkin et al. 2023). Spilker et al. (2020) also observed an outflow of molecular gas in this galaxy with $\dot{M}_{\mathrm{out}} \sim 150 M_\odot\ \mathrm{yr}^{-1}$. Finally, Peng et al. (2022) reported the presence of a star-forming ($>17\ M_\odot\ \mathrm{yr}^{-1}$) companion located within a projected distance of less than 5 kpc from the main galaxy, which could potentially influence the main galaxy.

The layout of this paper is as follows. In Section 2, we describe the data used for this analysis, and in Section 3, we present our analysis of the nearby companion. Hereafter, we designate the main galaxy SPT0418A and the companion galaxy SPT0418B. Next, in Section 4, we discuss the lens modeling and dynamical state of the system, conduct SED modeling, and estimate the stellar mass. In Section 5, we have our concluding remarks about the SPT0418−47 system and how a merger would affect our understanding of it. Throughout, we assume a Planck cosmology (Planck Collaboration et al. 2020): $H_0 = (67.4 \pm 0.5)$ km s^{-1} Mpc^{-1}, $\Omega_m = 0.315 \pm 0.007$, and $\Omega_\Lambda = 0.685 \pm 0.007$.

2. Data and Processing

2.1. JWST

Imaging observations of SPT0418−47 were taken by the NIRCam and MIRI instruments on 2022 August 11 and 2022 August 22, respectively, as part of the TEMPLATES program. Imaging was taken with filters spanning wavelengths from 1.15 to 21 μm, with the target centered in detector B4 for NIRCam. The filters and corresponding exposure times are given in the Appendix in Table 3.

J. R. Rigby et al. (2023, in preparation) describe in detail the data reduction process for TEMPLATES. Here we summarize the process for the subset of TEMPLATES data analyzed in this paper. Starting with the Level 2A data products for NIRCam, we applied a custom destriping algorithm to correct for 1/f noise and jumps between amplifiers. The destriped images were then run through the JWST pipeline (Version 1.8.2) using the CRDS context jwst_0988.pmap.

This version of the official JWST calibration was the most up-to-date at the time of this analysis, and is consistent to within 3% of the absolute flux calibration in Boyer et al. (2022).

For the MIRI imaging, we used a four-point dither pattern optimized for extended sources. Uncalibrated images were processed through the JWST pipeline version 1.9.5dev using the pmap jwst_1062.pmap. There are known striping issues for MIRI imaging, mainly arising from detector 1/f noise. We implemented destriping for the current data by creating a detector template using the four dither positions and removing it from each exposure after stage 2 of the pipeline.[28] These destriped stage 2 data products were processed through the stage 3 pipeline, and the images output from stage 3 were used for the analysis in this paper.

We realigned the MIRI and NIRCam imaging to a common frame to correct for residual astrometric offsets and generated a simulated point-spread function (PSF) for each filter for the date of observation, using WebbPSF version 1.0.1.dev126 +g6d83a9d (Perrin et al. 2012, 2014), given the measured wave front of the telescope, which is measured every two days (McElwain et al. 2023). Cutouts of SPT0418−47 in the F115W through F2100W filters are shown in Figure 1, illustrating the relative contrast between the lensing galaxy and the SPT0418−47 system as a function of wavelength.

[28] https://github.com/STScI-MIRI/Imaging_ExampleNB/blob/main/helpers/miri_clean.py

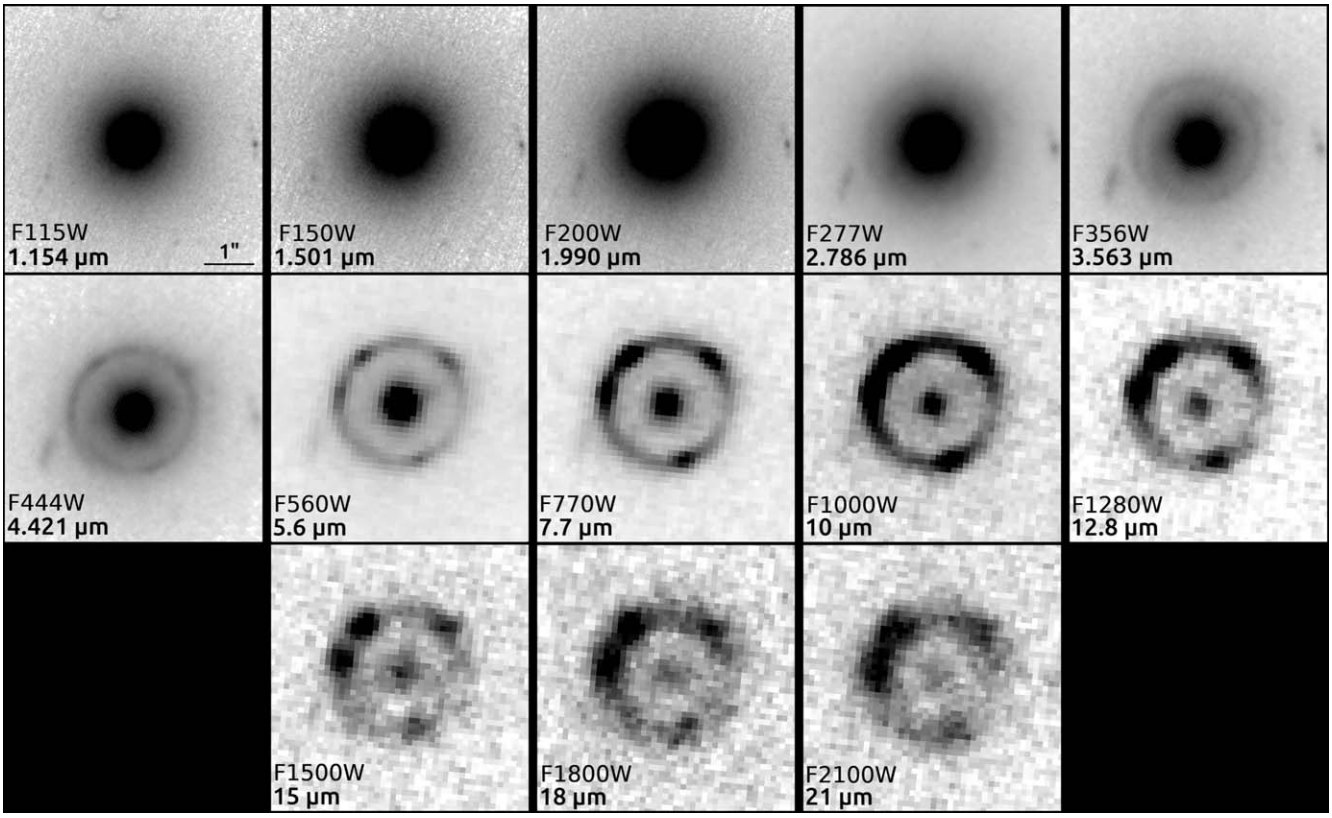

Figure 1. Images of SPT0418−47 in all 13 NIRCam and MIRI passbands ranging from 1.15 to 21 μm. These images illustrate the contrast as a function of wavelength between the foreground lens, SPT0418A, and SPT0418B. Specific locations of SPT0418B are shown in Figure 2. The JWST images are displayed with square root scaling. The minimum value of the flux density scale is set to 0.1 MJy sr^{-1} below sky; the maximum in each frame is 2 MJy sr^{-1} above the sky level. A 1″ scale bar is included in the upper left panel. Pivot wavelengths are labeled for each of the NIRCam filters, and central wavelengths are listed for the MIRI filters.

2.2. ALMA

We combine ALMA observations of the [C II] 158 μm line and underlying dust continuum observed in projects 2016.1.01374.S (PI: Y. Hezaveh) and 2016.1.01499.S (PI: C. Litke). Both projects used a similar correlator setup, centering the [C II] line in the upper sideband, while the lower sideband provides continuum data. The total on-source time between both projects was 4.9 hr. We performed a continuum subtraction in the uv-plane assuming a linear frequency dependence of the continuum emission, excluding frequencies with significant [C II] emission from the fit. Compared to Rizzo et al. (2020), who only used the data from 2016.1.01499.S project (PI: Litke), our combined observations have a four times smaller beam and a factor of 14 greater total on-source time.

The individual observing blocks from each project span a wide range in spatial resolution, from 0.″2 to 0.″15. We jointly imaged the data using natural weighting (accounting for the different phase centers and frequency setups of the two projects) using tclean in the CASA software package (McMullin et al. 2007; THE CASA TEAM et al. 2022). We imaged the [C II] emission using the continuum-subtracted data with a spectral resolution of 50 km s^{-1}. We base our analysis on images created by applying a 50 mas external taper in the uv-plane, which offers a reasonable compromise between spatial resolution and sensitivity and is well matched to the resolution of the NIRCam imaging. The final synthesized beam size was 93 mas × 97 mas, reaching a sensitivity of 0.20 mJy beam^{-1} in 50 km s^{-1} channels of the [C II] cube, after correcting for the primary beam response at the position of the lens. We produced flux-weighted mean velocity maps of the [C II] emission after masking pixels detected at <3σ significance.

3. Detection of the Multiply Imaged Companion

There are multiple sources near SPT0418A that could be physically associated if they lie at the same redshift. In this section, we investigate each of these sources, then perform a source plane reconstruction of SPT0418−47.

3.1. The Multiply Imaged Companion

The JWST imaging reveals in detail the stellar emission from SPT0418A. To better view SPT0418−47, we model and remove the flux from the foreground lens, which is an elliptical galaxy at z = 0.263. We use GALFIT (Peng et al. 2002, 2010) to fit a Sérsic bulge to the foreground lens at the wavelength of the F150W bandpass, convolving the model with the PSF from WebbPSF. In the model, we also add a secondary exponential disk component to improve the model in the central region of the galaxy. During the fitting, we mask nearby galaxies and use the error map to weight the fit. The best-fit χ^2 model for the bulge has n = 3.17 ± 0.02 and r_e = 0.″88 ± 0.″01, while the disk component has r_e = 0.″067 ± 0.″001 and contains 7% of the total light.

We take the best-fit in F150W, fix the axis ratios, position angles of the two components, and Sérsic parameters, and then model the lensing galaxy at the other wavelengths using the appropriate PSFs from WebbPSF. We allow the position, physical scale, and flux to be free parameters. The position is

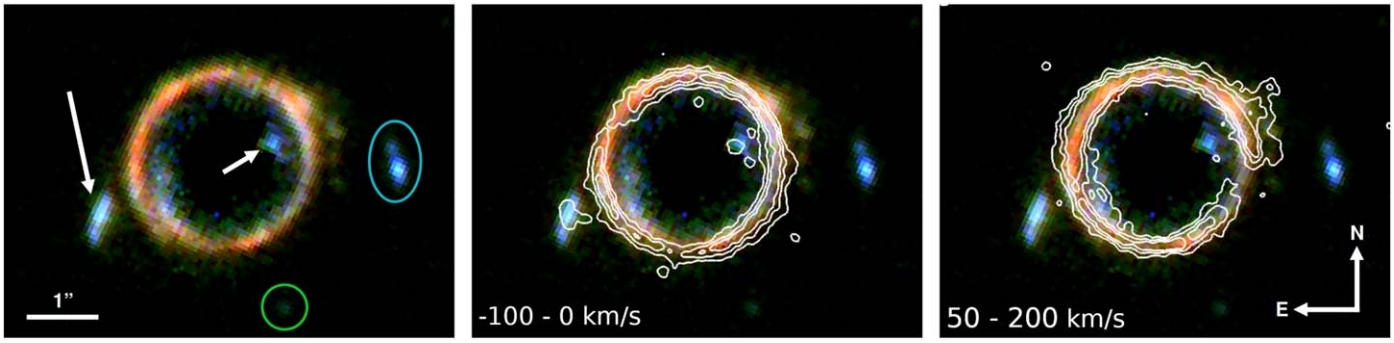

Figure 2. Residual color image of SPT0418−47 generated from the F277W, F356W, and F444W NIRCam imaging after modeling and removal of the foreground lens using GALFIT. The left panel shows SPT0418A and SPT0418B, with arrows denoting the two images of SPT0418B. Also circled in cyan and green are two additional potential companions investigated in Section 3.2 that are not detected in the ALMA data cube. [C II] contours at the rest frame of SPT0418−47 are overlaid on the NIRCam image in the center panel, integrated over the channels where the companion appears from −100 to 0 km s^{-1} relative to the redshift of SPT0418−47. The slight offsets between the ring and the contours in the center panel are due to the contours being integrated only over the channels where the companion appears strongly, rather than the whole ring. In the right panel, we show the [C II] contours integrated from 50 to 200 km s^{-1} relative to the redshift of SPT0418−47 to show the extended feature opposite the companion connected to the ring formed by the lensing of SPT0418A. The center of the region where the foreground lens was subtracted is masked because the statistical noise is high.

left free to account for any remaining subpixel astrometric offsets between images, while the physical scale is left free to account for radial color gradients.

In the left panel of Figure 2, we show a three-color image of the lensed galaxy after the removal of the foreground lens.[29] In this image, we can now see two bluer objects, one interior to the arc and the other exterior on the opposite side. This geometry is consistent with multiple lensed images of a single companion (SPT0418B), as discussed by Peng et al. (2022). The proximity of SPT0418A and SPT0418B in the image plane is suggestive of a small separation in the source plane.

The ALMA [C II] data also show clear emission signatures at the locations of the two images of SPT0418B. In the center panel of Figure 2, we present contours from the ALMA [C II] data, integrated from −100 to 0 km s^{-1} relative to the central velocity of SPT0418A, overlaid on the NIRCam imaging. This emission confirms that SPT0418B is very close to SPT0418A not only in the image plane, but also in velocity space. Both images of SPT0418B have consistent mean relative velocities of approximately −130 km s^{-1}.

3.2. Other Potential Companions

In addition to SPT0418B, there are two more objects visible only in the NIRCam filters at small angular separation. These objects, located at (04:18:39.4, −47:51:52.81) and (04:18:39.6, −47:51:54.76), are close enough that they would both have projected physical separations of ~10 kpc from SPT0418A if at the same redshift. These objects do not appear in the ALMA [C II] data, and photometric redshift estimates using CIGALE give redshifts of $z_{\rm phot} = 0.4 \pm 0.25$ and $z_{\rm phot} < 0.05$ for the west and south objects, respectively. We thus conclude that these objects lie in the foreground and are not associated with SPT0418A or SPT0418B.

4. Evidence for an Ongoing Merger

Given the projected proximity of SPT0418B, we next explore whether this system is an ongoing merger and attempt to constrain its physical parameters. We investigate the source plane reconstruction of SPT0418A and SPT0418B, the image plane kinematics of SPT0418B, and SED modeling and stellar mass estimates of both.

4.1. Source Plane Reconstruction

We perform source plane reconstruction using LENSTRONOMY (Birrer & Amara 2018; Birrer et al. 2021). LENSTRONOMY is capable of joint parametric fitting of the foreground lens mass distribution and flux distribution of the background source, enabling the simultaneous fitting of multiple photometric bands. Further, it can use "shapelets" (Refregier 2003; Refregier & Bacon 2003; Massey & Refregier 2005; Birrer et al. 2015), which are a series of 2D basis functions, to rapidly reconstruct the source plane without parametric models of the source light, so long as an accurate lens model is used. As a nonparametric method of source plane reconstruction, shapelets can reconstruct substructures that are missed by simple parametric models. Finally, LENSTRONOMY can add shapelets on top of parametric models of the source to find any additional substructure in the source plane without using many orders of shapelets for structures that are well described by parametric models.[30]

To model the global structure of the SPT0418−47 system, we start by using elliptical Sérsic profiles in the source plane. These simple models provide a good first-order fit to the profiles. To model the mass profile of the lensing galaxy, we use a singular isothermal ellipsoid with external shear. We perform multiband fitting of our GALFIT-subtracted data in F277W, F356W, F444W, F560W, and F770W. Starting with only the parametric profiles, we first presample the space using a particle swarm optimization (Kennedy & Eberhart 1995) to get near the solution while sampling the high-dimensional space quickly. We then use this approximate solution to seed the Markov Chain Monte Carlo (MCMC) sampler emcee (Foreman-Mackey et al. 2013), allowing it to run to convergence. We then add shapelets to the source model at

[29] We mask the noisy residual at the center of the foreground galaxy in this image.

[30] One feature of shapelets is that the final models can include regions with unphysical negative flux values. The presence of negative values is intrinsic to the shapelet approach. In the idealized case, the summation of the shapelets should result in a net positive flux at all locations, but when modeling with a limited number of shapelets, these unphysical negative flux values occur at some locations surrounding bright, positive features.

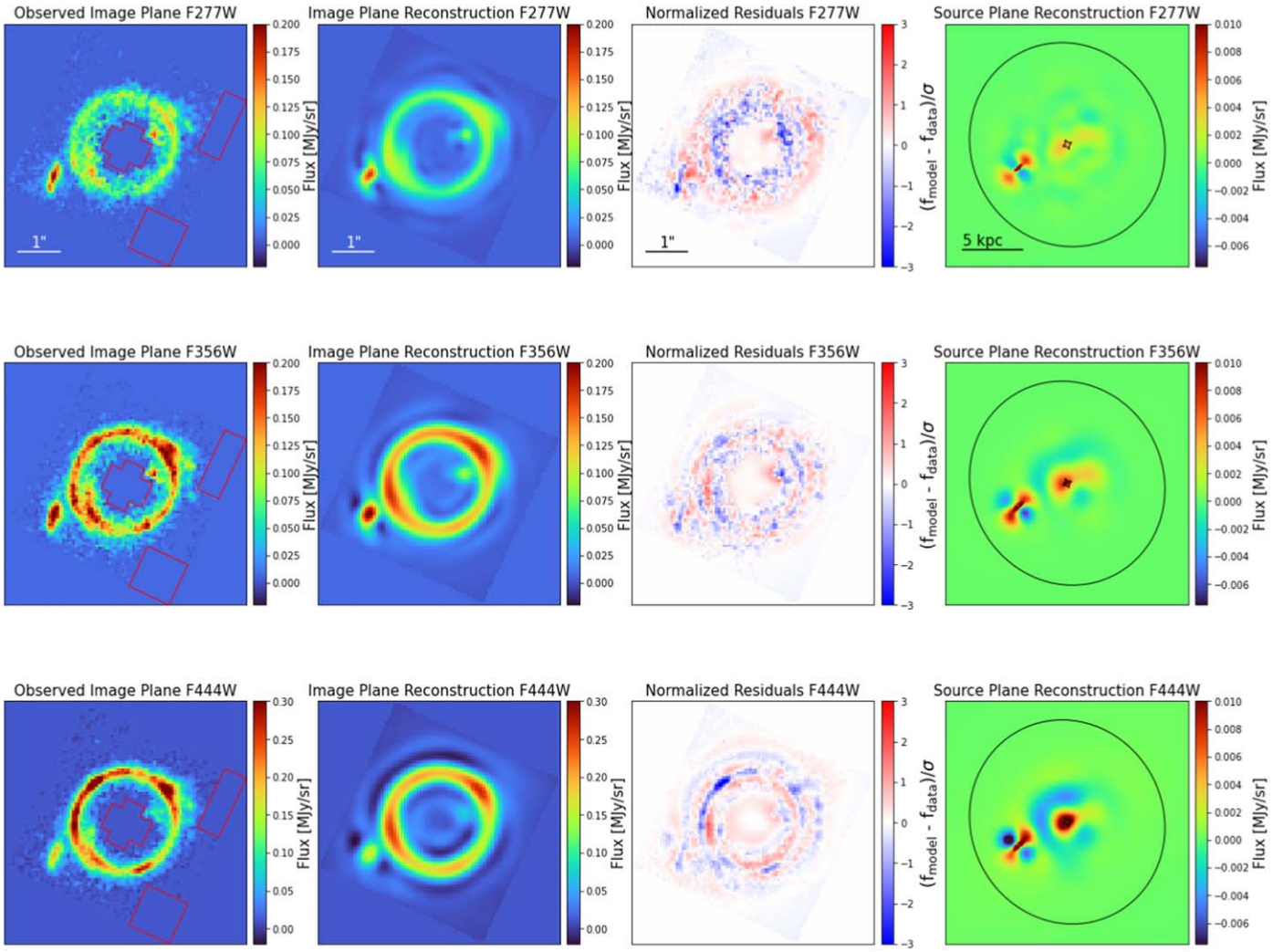

Figure 3. Source plane reconstruction of each band modeled using shapelets and parametric source models. Each row shows one of the three NIRCam bands use the modeling. The leftmost column shows the image plane shapelet reconstruction with the GALFIT-subtracted data. The second column displays the observed im plane of SPT0418−47, with regions masked out due to unassociated flux outlined in red. The third column provides the normalized image plane residuals after mo subtraction. We note that there is remaining small-scale structure that is not removed, because it is smaller that the smallest-scale shapelets used. The rightmost p shows the source plane reconstruction derived from the combination of parametric and shapely modeling, with the caustic and critical curve overlaid. All panels are rotated such that north is up and east is left. Due to the changing source structure with wavelength, we cannot use the same shapelet set for each band, but rather reconstruct each one separately, using the same mass model and initial source plane model.

each wavelength to better model any substructure for each image.

In this lens modeling, due to the prior GALFIT subtraction of the lens light, we found difficulty in modeling both SPT0418A and SPT0418B when including the background noise with LENSTRONOMY. In the future, it would be prudent to perform the lens light subtraction within the software used to conduct the lens modeling, rather than using two separate methods. As part of this modeling, we imposed a prior that all values below a threshold of 0.01σ less than the median are ignored relative to the pixel distribution in the region we are modeling. This prior forces LENSTRONOMY to consider only flux from regions with a higher signal-to-noise ratio (S/N), while ignoring pixels less than the threshold in the parametric model fitting.

From the source plane reconstruction, we find that the projected physical separation between the centers of the two galaxies is 4.42 ± 0.05 kpc. In modeling the source plane with pure Sérsic profiles, we are unable to reproduce some of the features in both SPT0418A and SPT0418B. By adding shapelets on top of these Sérsic profiles, we are able to reproduce those features in the image plane, leading to the reconstruction shown in Figure 3. Shapelets are useful in this reconstruction, as previous reconstructions (Hezaveh et al. 2013; Spilker et al. 2016; Rizzo et al. 2020) did not detect emission from regions poorly represented by parametric models, such as the tail-like features extending from both SPT0418A and SPT0418B. Shapelets are a quick way to model these new features, building on parametric models without doing a full pixelated reconstruction.

Figure 3 shows the lens model in the F356W filter, a band in which both SPT0418B and the extended structure associated with SPT0418A can be clearly seen. We list the parameters for the lens model of this system in Table 1, along with the estimated uncertainties. We note that the derived θ_E is consistent with Rizzo et al. (2020) to within the uncertainties, and slightly lower than what is found in Spilker et al. (2016).

Next, we use the parametric lens mass model listed in Table 1 to generate a backward ray tracing of the system. This approach provides an alternative to the joint parametric

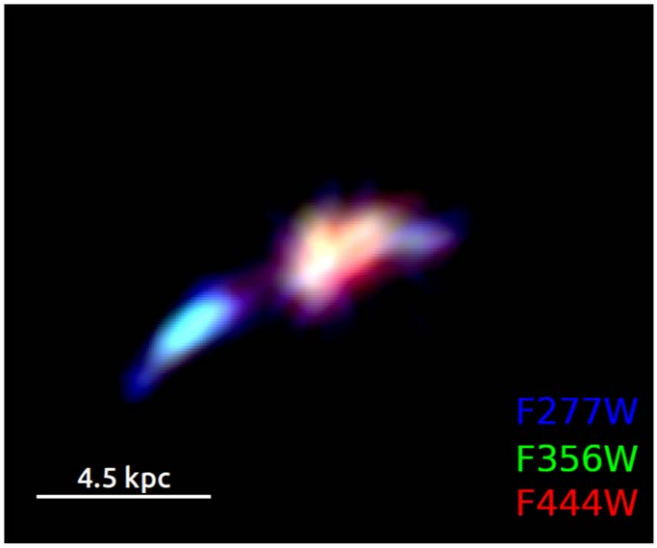

Figure 4. We show a source plane reconstruction generated using backward ray tracing. We produce this reconstruction using the F277W, F356W, and F444W filters as in Figure 2. The dust-obscured galaxy SPT0418A is on the right, and the bluer SPT0418B is on the left.

Table 1
Lens Model Parameters

Parameter	Model Value[a]
θ_E	1.″207 ± 0.″002
$\grave{o}_1$	−0.031 ± 0.006
$\grave{o}_2$	0.061 ± 0.009
x_{Lens}	−0.010 ± 0.003
y_{Lens}	−0.003 ± 0.002
γ_1	−0.005 ± 0.003
γ_2	−0.007 ± 0.004

Note.
[a] Uncertainties are estimated taking the average of the 16th and 84th percentiles from the marginalized distributions of the MCMC. LENSTRONOMY parameters are defined as follows: θ_E is the circularized Einstein radius, and $\grave{o}_2$ are the x- and y-components to the ellipticity, x_{Lens} and y_{Lens} are the offset from the center of the image in arcseconds, and γ_1 and γ_2 are the external shear components. The orientation of this model is in the native orientation of the NIRCam detector, with rotations introduced afterward to avoid introducing autocorrelation noise. The rotation from the NIRCam detector orientation to north up is 245° clockwise.

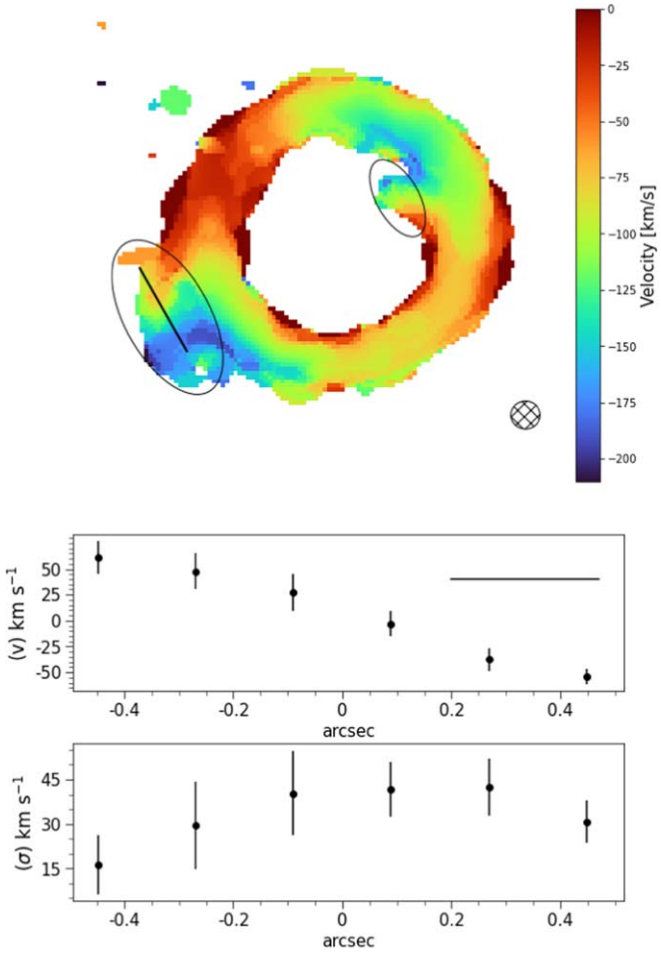

Figure 5. The upper panel shows an ALMA velocity map of the SPT0418−47 system, scaled to highlight the internal velocity gradient of SPT0418B. The two ellipses are the regions where emission from SPT0418B is expected, and the area within these two ellipses shows mirrored velocity gradients, as expected from the lensing geometry. In the bottom right, we show the beam size as the crosshatched ellipse. The velocity range is displayed from −200 to 0 km s^{-1} relative to the redshift of SPT0418A, as reported in Reuter et al. (2020). The middle panel shows the extracted rotation curve from the southeast image of SPT0418B, along the line shown in the first panel. The bottom panel shows the extracted velocity dispersion along the same line in the top panel. The horizontal line in the middle panel is the size of the beam—both the velocity and dispersion profiles are sampled more finely than the synthesized beam size.

shapelet fitting shown in Figure 3 for assessing the presence of additional structures. We take the NIRCAM F277W, F356W, and F444W imaging and map it back to the source plane, accounting for magnifications of the multiple images to create the source plane reconstruction. The result is shown in Figure 4. In this figure, we again see some extended structure in the light distribution, consistent with that inferred from the shapelets. Further, we can see color gradients across both SPT0418A and SPT0418B. For SPT0418A, we can see the core region, which appears white in this color mapping, corresponding to the quadruply imaged clump most visible in the MIRI bands. This region then extends outward into a larger red structure that has higher extinction. The tail feature extending from SPT0418A to the northwest in Figure 4 appears blue, just as it does in the image plane color composite shown in Figure 2. Similar tidal features have been found in previous studies (Messias et al. 2014; Rybak et al. 2020) of other DSFGs.

4.2. Image Plane Kinematics of SPT0418B

We create a velocity moment map from the [C II] data in Figure 5 to investigate whether the kinematic signatures are also consistent with our prediction of images from our lensing reconstruction, and investigate the image plane kinematics. Internal gradients are visible in both SPT0418A and SPT0418B. As highlighted by the ellipses in Figure 5, the velocity gradients for the two images of SPT0418B are equal and mirrored, as must be true if we are observing multiple images of the galaxy.

A rotation curve and velocity dispersion are extracted for the southeast image of the companion along the line shown in Figure 5. From this figure, we see that the velocity and dispersion profiles for SPT0418B are consistent with a galaxy

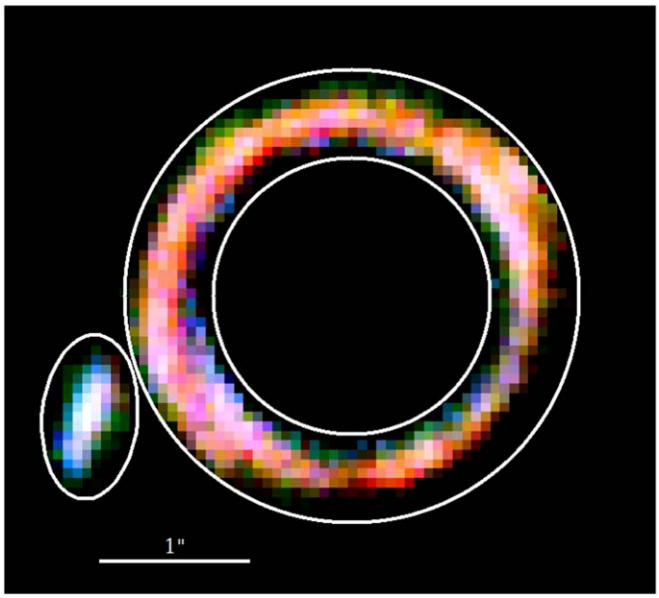

Figure 6. Apertures used for photometric extraction for SPT0418A and SPT0418B. The inner image of SPT0418B was not used to extract photometry because it is more sensitive to residuals from the subtraction of the lensing galaxy than the outer image.

that exhibits ordered rotation but is dynamically hot. Rizzo et al. (2020) found a dynamically cold disk for SPT0418A using a kinematically driven reconstruction method with a V/σ ratio of 9.7 ± 0.4, though this reconstruction appears to not include emission from both SPT0418B and the tail feature seen in SPT0418A.

4.3. Stellar Mass Ratios

We next compare the stellar masses of the two components. We use the lens model from above (Table 1) to derive the magnifications of SPT0418A and SPT0418B. We find total magnifications of $\mu = 29 \pm 1$ for SPT0418A and $\mu = 4.1 \pm 0.7$ for SPT0418B. The uncertainties on the magnifications are derived from 100 random draws of the MCMC, calculating the flux in the image and source plane reconstructions of the parametric model. The multiple images of SPT0418B have effective magnifications of $\mu = 1.2 \pm 0.3$ and $\mu = 2.9 \pm 0.6$ for the inner and outer images, respectively. For SPT0418B, we use only the data for the source exterior to the SPT0418A ring to minimize photometric uncertainties due to overlap with the ring. Further, we use the annular aperture shown in Figure 6 to find the magnification of SPT0418A in the image plane. We only use the parametric Sérsic profiles to calculate these magnifications, allowing us to avoid any unphysical negative fluxes that arise intrinsically as part of the shapelet process. The difference in the calculated magnification from band to band is less than the quoted uncertainty for SPT0418A and SPT0418B.

To compare the stellar masses of SPT0418A and SPT0418B, we extract the photometry for each using fixed photometric apertures. Figure 6 shows the apertures used for each component. These apertures are designed to be large enough that there is minimal differential flux loss due to the wavelength dependence of the PSF. The flux densities derived for each source are presented in the Appendix in Table 3. Reuter et al. (2020) also provide 100 μm–3 mm SPT, LABOCA, Herschel/SPIRE, ALMA, and Herschel/PACS data for SPT0418−47. These flux densities include contributions from both SPT0418A and SPT0418B. From the ALMA data, we measure 96% ± 2% of the flux as being associated with SPT0418A. When fitting the SED for SPT0418A, we include this fraction of the flux density for all bands measured by Reuter et al. (2020). The differences in SFR and stellar mass between using this fractional flux and using the total flux are smaller than the statistical uncertainties.

We use both CIGALE (Boquien et al. 2019) and PROSPECTOR (Johnson et al. 2021) to fit the SEDs. This provides a measure of the systematic uncertainties associated with the assumptions in the SED modeling. CIGALE is an SED fitting code commonly used for DSFGs that simultaneously models UV–far-IR (FIR) emission of galaxies, including prescriptions for stellar-age-dependent dust attenuation in the UV and dust emission in the IR. PROSPECTOR performs similarly, but allows for greater flexibility when modeling the star formation history (SFH) of a galaxy, by accepting nonparametric solutions. For both codes, we assume a Chabrier initial mass function (Chabrier 2003). For both codes, we use a flexible attenuation curve parameterization that allows for a variable UV–optical slope and V-band attenuation; specifically, CIGALE uses the parameterization from Boquien et al. (2019) and PROSPECTOR that of Kriek & Conroy (2013). The metallicity is allowed to vary for SPT0418A, and we apply a uniform prior on the metallicity between 80% and 125% of solar, consistent with De Breuck et al. (2019; $0.3 < Z/Z_e < 1.3$), and based on our team's spectroscopic analysis (Birkin et al. 2023).

For SPT0418B, we set a uniform prior between 65% and 75% solar on the metallicity for PROSPECTOR based upon the NIRSpec analysis of Birkin et al. (2023). We fix the metallicity to solar for CIGALE, as this is the closest metallicity value available in the code. With CIGALE, we model the SFH parametrically as an exponential decay ($\tau = 1$ Gyr), with an additional burst component using the Bruzual & Charlot (2003) stellar population model. In contrast, PROSPECTOR uses Flexible Stellar Population Synthesis stellar population modeling (Conroy et al. 2009; Conroy & Gunn 2010), and we allow a nonparametric SFH with a Dirichlet prior on the mass formed per time bin (Leja et al. 2019). Lower et al. (2020) demonstrated with simulations that such an approach can outperform parametric models. The PROSPECTOR fit also permits a nonuniform dust screen, and we let the fractional obscuration be a free parameter (Lower et al. 2022). The posterior for the obscured fraction peaks at >98% for SPT0418A; however, the small amount of light that is unobscured is important in the SED fit.

In Figure 7, we show the SED models that best fit our data with each code for both SPT0418A and SPT0418B. Similarly, the derived quantities from these SED models are presented in Table 2. The constraints on SPT0418B are less robust due to the more limited set of photometric detections, since this source is relatively faint and the MIRI integration times are short. For PROSPECTOR, we plot the median and 1σ spread in the model SEDs, and for CIGALE, we plot the model corresponding to the minimum χ^2.[31] For PROSPECTOR, we find that it fits the FIR dust emission poorly. Thus, we had PROSPECTOR model only the stellar emission of the SED, so as not to have improper dust models bias the fit. The reduced χ^2 statistics for the PROSPECTOR fits to the SPT0418A and SPT0418B SEDs are

[31] CIGALE does not calculate the 1σ spread in model SEDs.

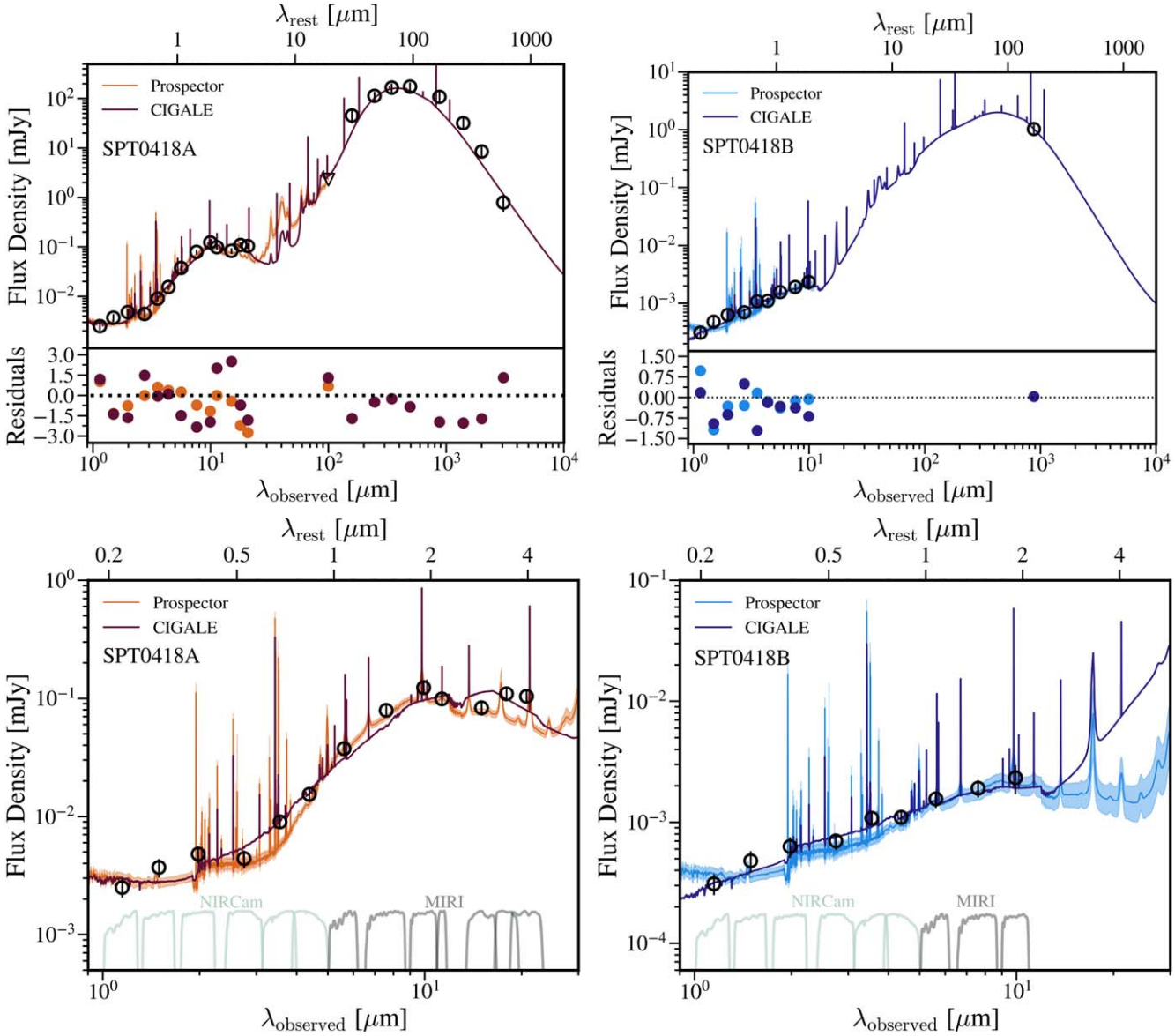

Figure 7. Top: UV–FIR SEDs for SPT0418A (left) and SPT0418B (right), with observed photometry not corrected for magnification. The best-fit models from PROSPECTOR and CIGALE are shown as shaded bands and solid curves, respectively. The PROSPECTOR SED is the median model SED, with the 16th–84th percentiles shown in the shaded regions, while the best-fit CIGALE SED is the model corresponding to the minimum χ^2. The corresponding model parameters can be found in Table 2. Bottom: zoom-ins to the rest-frame UV and optical.

3.42 and 0.54, respectively, and 3.35 and 0.48 when fit with CIGALE. The differences in the χ^2 values between the two sources are caused by both the numbers of observations and models. Since SPT0418B only has one data point in the FIR, it overfits the point for all of the FIR emission.[32]

A comparison of the results from the two SED modeling codes in Table 2 shows that the derived SFRs and effective A from PROSPECTOR and CIGALE are consistent within the uncertainties for both SPT0418A and SPT0418B. The inferred stellar metallicity for the main source is consistent with the solar value we have assumed in the CIGALE model.

The most significant discrepancy between the two codes is with the inferred stellar mass. For SPT0418A, PROSPECTOR infers a magnification-corrected stellar mass of $3.5^{+1.4}_{1.4} \times 10^{10}$, which is a factor of 2.3 times larger than the CIGALE median stellar mass value of $1.5 \pm 0.6 \times 10^{10} M_e$. This increases to a factor of 4.1 for SPT0418B, for which PROSPECTOR yields $8.2^{+3.6}_{3.0} \times 10^{9} M_e$ compared to $2.02 \pm 0.9 \times 10^{9} M_e$ for CIGALE. These differences in the inferred stellar masses are largely driven by the different models for the SFH. In CIGALE, we assumed a declining exponential SFH (τ_{best} = 1 Gyr) with a burst component, inferring 80% of the galaxy's stellar mass as being formed in the recent burst. The nonparametric SFH model we used in PROSPECTOR does not a priori assume a shape for the SFH; rather, it fits for the stellar mass formed in each bin and estimates that 33% of the total galaxy stellar mass was formed in a recent burst, with a significant fraction of the stellar mass having formed at earlier times. This difference highlights that caution should be exercised when comparing stellar mass estimates in the literature that use different codes and input assumptions (see also Michałowski et al. 2014;

[32] We note that the χ^2 values for the two SED fitting packages are not directly comparable, because the codes use different methodologies to find the best-fit SEDs.

Table 2
SED Modeling Results

Source	Magnification (μ)	Code	Stellar Mass (μM_e)	SFR_{100} (μM_e yr^{-1})	Z_* (Z_e)	A_V	sSFR (10^{-9} M_e yr^{-1})
SPT0418A	29.5 ± 1.2	PROSPECTOR	$10.2^{+3.4}_{-1.9} \times 10^{11}$	4257^{+989}_{-742}	$0.94^{+0.15}_{-0.11}$	$3.75^{+0.12}_{-0.14}$	$4.2^{+1.0}_{-0.7}$
		CIGALE	$4.5 \pm 0.9 \times 10^{11}$	3770 ± 545	1	3.8 ± 0.1	8.4 ± 1.2
SPT0418B	2.92 ± 0.63	PROSPECTOR	$23.9^{+9.1}_{-7.2} \times 10^{9}$	$25.3^{+23.6}_{-15.2}$	$0.68^{+0.04}_{-0.02}$	$1.5^{+0.32}_{-0.43}$	$1.1^{+1.1}_{-0.7}$
		CIGALE	$5.9 \pm 2.6 \times 10^{9}$	43.6 ± 17.9	1	1.4 ± 0.2	7.4 ± 4.4

Note. The quoted parameter results are values without any magnification correction. The CIGALE models assume a fixed stellar metallicity value set to Z_e, as this code only permits a few discrete values.

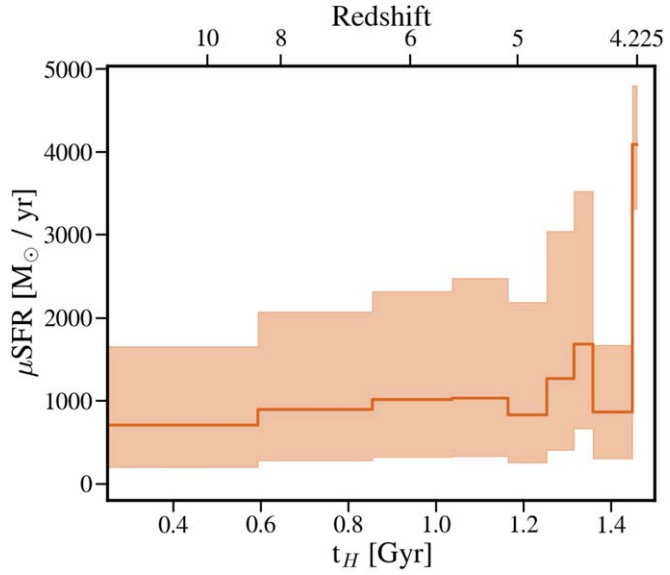

Figure 8. SFH as found by PROSPECTOR for SPT0418A, with 1σ uncertainties shown in the shaded region. This shows a relatively constant SFH over the history of SPT0418A with a factor of ~4 increase in the SFR between 100 Myr before the observed time and the observed time. This could be caused by the merger, though that is difficult to causally prove.

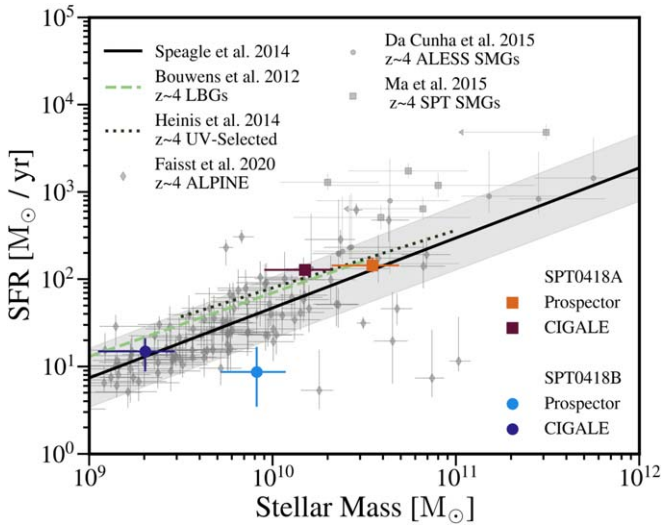

Figure 9. A comparison of SPT0418A (orange—PROSPECTOR; maroon—CIGALE) and SPT0418B (light blue—PROSPECTOR; navy—CIGALE) to the main sequence of star-forming galaxies. The coloration shows the placement for both for PROSPECTOR and CIGALE, with the same colors as Figure 7. SPT0418 is compared to z ~ 4 galaxies from da Cunha et al. (2015), Ma et al. (2015), and Faisst et al. (2020), fits to selected galaxy samples from Heinis et al. (2014) and Bouwens et al. (2012), and the predicted z = 4.225 main-sequence relation from Speagle et al. (2014).

Mobasher et al. 2015; Hunt et al. 2019). We have verified that if we require the SFH to be the same in both codes, then the two codes give consistent results.

Setting aside the offset between the two codes for the derived stellar masses, the ratio of the stellar masses for SPT0418A and SPT0418B is consistent between the two codes. Accounting for magnification, the inferred true stellar mass ratios are $4.2^{+1.9}_{-1.6}$ for PROSPECTOR and 7.5 ± 3.7 for CIGALE, respectively. The uncertainties are large, but they still enable us to conclude that this system is consistent with being a ~4 to 1 ongoing minor merger between the two galaxies. In this context, the extended structure associated with SPT0418A is potentially a tidal feature arising from the interaction.

It is interesting to consider the effect of this merger upon the stellar populations in these galaxies. Rizzo et al. (2020) found a dynamically ordered disk in SPT0418A, which would argue that the interaction has not significantly influenced the internal dynamics. We consider the sSFR and SFH as tests for this picture. The nonparametric SFH from PROSPECTOR suggests a minimally variable SFH over 1 Gyr of evolution, with an average (magnification-corrected) rate of 32 M_e yr^{-1}. Then, in the last 10 Myr, the SFR jumps to 138 M_e yr^{-1}—a factor of 4 increase—resulting in the formation of ~33% of the total stellar mass of the system (see Figure 8). We caution that determining the exact contribution of the stellar mass formed in the recent burst to the total stellar mass is moderately model-dependent and prone to issues like newly formed O- and B-type stars dominating the luminosity rather than the older stellar population (outshining; Papovich et al. 2001; Narayanan et al. 2023) and the difficulty of determining multiple episodes of star formation (Iyer et al. 2019). This SFH model, however, suggests that the merger has induced significant recent star formation, even if this is not apparent from a broad comparison of the sSFR to the main-sequence population. In Figure 9, we compare the sSFRs for SPT0418A and SPT0418B with estimates for the star-forming main sequence at z = 4 from Bouwens et al. (2012) for UV-dropout Lyman-break galaxies (see Figure 9), from da Cunha et al. (2015) for ALESS galaxies, from Faisst et al. (2020) for ALPINE galaxies, and from Speagle et al. (2014) for a compilation of literature samples. The sSFR of SPT0418B is also $< 10^{-8}$ yr^{-1} from both codes, comparable to the typical values found for star-forming galaxies at this redshift (see Heinis et al. 2014 and references therein). The sSFRs of both SPT0418A and SPT0418B appear to not (yet) be significantly elevated relative to the main sequence in this comparison. In da Cunha et al. (2015), the multiplicity fraction of the systems was previously identified in Hodge et al. (2013). Of the 2.5 ≤ z < 4.5 galaxies that appear

to have multiple sources, the majority do not appear to be significantly elevated off the main sequence.

The sSFR of SPT0418A therefore appears to not be significantly elevated by the merger; indeed, the location of SPT0418A on the M–SFR plane is within the 1σ scatter of the z = 4 main-sequence relation from Speagle et al. (2014).

5. Conclusions

In this paper, we have used JWST NIRCam and MIRI imaging of SPT0418−47, which is at a redshift z = 4.225, from the TEMPLATES ERS program to investigate the unlensed properties of the SPT0418−47 system. We have analyzed the stellar emission from both SPT0418A and the multiply imaged companion galaxy (SPT0418B), deriving a lensing model and determining stellar masses. [C II] data from ALMA confirm that SPT0418B lies at the same redshift as SPT0418A, which was also reported in Peng et al. (2022), and exhibits a velocity gradient consistent with internal rotation.

From our lensing model reconstruction of the source plane, we determine the projected physical offset between the centroids of SPT0418A and SPT0418B. We measure a value of 4.42 ± 0.05 kpc in the source plane, which is broadly consistent with the estimate of Peng et al. (2022). We also see tentative evidence for extended features associated with SPT0418A in both JWST and ALMA. The ALMA data also demonstrate that the mean velocity offset between the two galaxies is 130 ± 10 km s^{-1}. Fits to the SEDs of both sources using both PROSPECTOR and CIGALE indicate that the stellar mass ratio of the two galaxies is approximately between 4 and 7–4.2$^{+1.9}_{1.6}$ for PROSPECTOR and 7.5 ± 3.7 for CIGALE. The simplest interpretation of these results is that we are witnessing an ongoing minor merger in this system. Despite this merger, there is no evidence for elevated sSFRs in either galaxy. Thus, the two galaxies are consistent with the star formation main sequence at their redshift. After applying the magnification correction, we find that SPT0418A has a stellar mass of $M_{\star} = 3.4^{+1.4}_{1.4} \times 10^{10}$ M$_e$ from PROSPECTOR or M$_a$ = 1.5 ± 0.6 × 10^{10} M$_e$ from CIGALE, and SPT0418B has a stellar mass of $M_{\star} = 8.2^{+3.6}_{3.0} \times 10^{9}$ M$_e$ from PROSPECTOR or M$_a$ = 2.02 ± 0.9 × 10^9 M$_e$ from CIGALE. The differences between these two codes are due to the different assumptions for SFHs found by each.

Finally, we have compared the results of fitting the SEDs with PROSPECTOR and CIGALE. The two codes yield similar SFRs, effective extinctions (Table 2), and stellar mass ratios. PROSPECTOR, however, yields stellar masses that are system-atically higher by factors of ~2–4.

Acknowledgments

This work is based in part on observations made with the NASA/ESA/CSA JWST. The data were obtained from the Mikulski Archive for Space Telescopes at the Space Telescope Science Institute, which is operated by the Association of Universities for Research in Astronomy, Inc., under NASA contract NAS 5-03127 for JWST. The specific observations analyzed can be accessed via doi: 10.17909/b0kt-xa31. These observations are associated with ERS program #1355. We express our gratitude to the thousands of people around the world who brought to fruition JWST and its science instruments NIRCam and MIRI.

The SPT is supported by the NSF through grant OPP-1852617. This paper makes use of the following ALMA data: ADS/NSF.ALMA#2016.1.01374.S and #2016.1.01499.S. ALMA is a partnership of ESO (representing its member states), NSF (USA) and NINS (Japan), together with NRC (Canada), MOST and ASIAA (Taiwan), and KASI (Republic of Korea), in cooperation with the Republic of Chile. The Joint ALMA Observatory is operated by ESO, AUI/NRAO, and NAOJ. The National Radio Astronomy Observatory is a facility of the National Science Foundation operated under cooperative agreement by Associated Universities, Inc.

Support for this program was provided by NASA through a grant from the Space Telescope Science Institute (JWST-ERS-01355), which is operated by the Association of Universities for Research in Astronomy, Inc., under NASA contract NAS 5-03127. M.A. acknowledges support from FONDECYT grant 1211951 and CONICYT + PCI + INSTITUTO MAX PLANCK DE ASTRONOMIA MPG190030. D.P.M., J.D.V., and K.P. acknowledge support from the US NSF under grants AST-1715213 and AST-1716127. M.A. and M.S. acknowl-edge support from CONICYT + PCI + REDES 190194 and ANID BASAL project FB210003. D.N. was supported by the NSF via AST-1909153. K.A.P. is supported by the Center for Astro Physical Surveys at the National Center for Super-computing Applications as an Illinois Survey Science Graduate Fellow. N.S. is a member of the International Max Planck Research School (IMPRS) for Astronomy and Astrophysics at the Universities of Bonn and Cologne.

Appendix
Photometry

We present the photometric data used for modeling the SEDs in Figure 7. Table 3 includes the JWST photometry from NIRCam and MIRI, while Table 4 summarizes the longer-wavelength literature fluxes from Reuter et al. (2020). The values in Table 4 correspond to the total flux from SPT0418A and SPT0418B. As discussed in the text, when fitting the SEDs for the two components, we assign 95.8% ± 2.2% of the flux in

Table 3
NIRCam and MIRI Data

Filter	λ[a] (μm)	Δλ (μm)	Int. Time (s)	SPT0418A (μJy)	SPT0418B (μJy)
F115W	1.154	0.225	687	2.5 ± 0.2	0.31 ± 0.03
F150W	1.501	0.318	343	3.7 ± 0.3	0.48 ± 0.05
F200W	1.990	0.461	429	4.8 ± 0.3	0.63 ± 0.06
F277W	2.786	0.672	687	4.4 ± 0.3	0.70 ± 0.04
F356W	3.563	0.787	343	9.0 ± 0.2	1.08 ± 0.03
F444W	4.421	1.024	429	15.4 ± 0.2	1.10 ± 0.04
F560W	5.6	1.2	277	37.5 ± 0.5	1.56 ± 0.09
F770W	7.7	2.2	144	79.1 ± 0.9	1.91 ± 0.12
F1000W	10	2.0	111	123.3 ± 2.2	2.33 ± 0.39
F1280W	12.8	2.4	111	98.9 ± 1.4	L
F1500W	15	3.0	111	83.1 ± 3.3	L
F1800W	18	3.0	222	109.3 ± 3.6	L
F2100W	21	5.0	832	104.1 ± 3.4	L

Notes. The quoted flux densities are observed values without any magnification correction. The fluxes for SPT0418B are for the outer image alone. See Section 4.3 for more details on the photometry measurements.
[a] For NIRCam, λ refers to the pivot wavelength, while for MIRI, λ is simply the central wavelength.

Table 4
Published SPT0418−47 FIR Photometry from Reuter et al. (2020)

λ (μm)	Flux Density (mJy)
100	<7
160	45 ± 8
250	114 ± 6
350	166 ± 6
500	175 ± 7
870	108 ± 11
1400	32 ± 5
2000	9 ± 1
3000	0.79 ± 0.14

the FIR bands to SPT0418A. This percentage corresponds to the fraction of the flux associated with SPT0418A in the ALMA imaging, and we assume the same fractional contribution for the other FIR observations.

ORCID iDs

Jared Cathey https://orcid.org/0000-0002-4657-7679
Anthony H. Gonzalez https://orcid.org/0000-0002-0933-8601
Sidney Lower https://orcid.org/0000-0003-4422-8595
Kedar A. Phadke https://orcid.org/0000-0001-7946-557X
Justin Spilker https://orcid.org/0000-0003-3256-5615
Manuel Aravena https://orcid.org/0000-0002-6290-3198
Matthew Bayliss https://orcid.org/0000-0003-1074-4807
Jack E. Birkin https://orcid.org/0000-0002-3272-7568
Simon Birrer https://orcid.org/0000-0003-3195-5507
Scott Chapman https://orcid.org/0000-0002-8487-3153
Håkon Dahle https://orcid.org/0000-0003-2200-5606
Christopher C. Hayward https://orcid.org/0000-0003-4073-3236
Yashar Hezaveh https://orcid.org/0000-0002-8669-5733
Taylor A. Hutchison https://orcid.org/0000-0001-6251-4988
Keunho J. Kim https://orcid.org/0000-0001-6505-0293
Guillaume Mahler https://orcid.org/0000-0003-3266-2001
Daniel P. Marrone https://orcid.org/0000-0002-2367-1080
Desika Narayanan https://orcid.org/0000-0002-7064-4309
Alexander Navarre https://orcid.org/0000-0001-7548-0473
Cassie Reuter https://orcid.org/0000-0001-7477-1586
Jane R. Rigby https://orcid.org/0000-0002-7627-6551
Keren Sharon https://orcid.org/0000-0002-7559-0864
Manuel Solimano https://orcid.org/0000-0001-6629-0379
Nikolaus Sulzenauer https://orcid.org/0000-0002-3187-1648
Joaquin Vieira https://orcid.org/0000-0001-7192-3871
David Vizgan https://orcid.org/0000-0001-7610-5544

References

Alaghband-Zadeh, S., Chapman, S. C., Swinbank, A. M., et al. 2012, MNRAS, 424, 2232
Baugh, C. M., Cole, S., & Frenk, C. S. 1996, MNRAS, 283, 1361
Birkin, Jack E., Hutchison, Taylor A., Welch, Brian, et al. 2023, ApJ, 958, 64
Birrer, S., & Amara, A. 2018, PDU, 22, 189
Birrer, S., Amara, A., & Refregier, A. 2015, ApJ, 813, 102
Birrer, S., Shajib, A., Gilman, D., et al. 2021, JOSS, 6, 3283
Boquien, M., Burgarella, D., Roehlly, Y., et al. 2019, A&A, 622, A103
Bouwens, R. J., Illingworth, G. D., Oesch, P. A., et al. 2012, ApJ, 754, 83
Boyer, M. L., Anderson, J., Gennaro, M., et al. 2022, RNAAS, 6, 191
Bruzual, G., & Charlot, S. 2003, MNRAS, 344, 1000
Chabrier, G. 2003, PASP, 115, 763
Conroy, C., & Gunn, J. E. 2010, ApJ, 712, 833
Conroy, C., Gunn, J. E., & White, M. 2009, ApJ, 699, 486
da Cunha, E., Walter, F., Smail, I. R., et al. 2015, ApJ, 806, 110
De Breuck, C., Weiß, A., Béthermin, M., et al. 2019, A&A, 631, A167
Engel, H., Tacconi, L. J., Davies, R. I., et al. 2010, ApJ, 724, 233
Faisst, A. L., Schaerer, D., Lemaux, B. C., et al. 2020, ApJS, 247, 61
Foreman-Mackey, D., Hogg, D. W., Lang, D., & Goodman, J. 2013, PASP, 125, 306
Governato, F., Brook, C. B., Brooks, A. M., et al. 2009, MNRAS, 398, 312
Hayward, C. C., Kereš, D., Jonsson, P., et al. 2011, ApJ, 743, 159
Heinis, S., Buat, V., Béthermin, M., et al. 2014, MNRAS, 437, 1268
Hezaveh, Y. D., Marrone, D. P., Fassnacht, C. D., et al. 2013, ApJ, 767, 132
Hodge, J. A., Karim, A., Smail, I., et al. 2013, ApJ, 768, 91
Hopkins, P. F., Bundy, K., Croton, D., et al. 2010, ApJ, 715, 202
Hopkins, P. F., Hernquist, L., Cox, T. J., & Kereš, D. 2008, ApJS, 175, 356
Hunt, L. K., De Looze, I., Boquien, M., et al. 2019, A&A, 621, A51
Iyer, K. G., Gawiser, E., Faber, S. M., et al. 2019, ApJ, 879, 116
Johnson, B. D., Leja, J., Conroy, C., & Speagle, J. S. 2021, ApJS, 254, 22
Kennedy, J., & Eberhart, R. 1995, in Proc. ICNN'95—Int. Conf. on Neural Networks 4, Particle Swarm Optimization, 1942
Kriek, M., & Conroy, C. 2013, ApJL, 775, L16
Leja, J., Carnall, A. C., Johnson, B. D., Conroy, C., & Speagle, J. S. 2019, ApJ, 876, 3
Litke, K. C., Marrone, D. P., Spilker, J. S., et al. 2019, ApJ, 870, 80
Lower, S., Narayanan, D., Leja, J., et al. 2020, ApJ, 904, 33
Lower, S., Narayanan, D., Leja, J., et al. 2022, ApJ, 931, 14
Ma, J., Gonzalez, A. H., Spilker, J. S., et al. 2015, ApJ, 812, 88
Marrone, D. P., Spilker, J. S., Hayward, C. C., et al. 2018, Natur, 553, 51
Massey, R., & Refregier, A. 2005, MNRAS, 363, 197
McElwain, M. W., Feinberg, L. D., Perrin, M. D., et al. 2023, PASP, 135, 058001
McMullin, J. P., Waters, B., Schiebel, D., Young, W., & Golap, K. 2007, in ASP Conf. Ser. 376, Astronomical Data Analysis Software and Systems XVI, ed. R. A. Shaw, F. Hill, & D. J. Bell (San Francisco, CA: ASP), 127
Messias, H., Dye, S., Nagar, N., et al. 2014, A&A, 568, A92
Michałowski, M. J., Hayward, C. C., Dunlop, J. S., et al. 2014, A&A, 571, A75
Mobasher, B., Dahlen, T., Ferguson, H. C., et al. 2015, ApJ, 808, 101
Narayanan, D., Lower, S., Torrey, P., et al. 2024, ApJ, 961, 73
Narayanan, D., Turk, M., Feldmann, R., et al. 2015, Natur, 525, 496
Papovich, C., Dickinson, M., & Ferguson, H. C. 2001, ApJ, 559, 620
Peng, Bo, Vishwas, Amit, Stacey, Gordon, et al. 2023, ApJL, 944, L36
Peng, C. Y., Ho, L. C., Impey, C. D., & Rix, H.-W. 2002, AJ, 124, 266
Peng, C. Y., Ho, L. C., Impey, C. D., & Rix, H.-W. 2010, AJ, 139, 2097
Perrin, M. D., Sivaramakrishnan, A., Lajoie, C.-P., et al. 2014, Proc. SPIE, 9143, 91433X
Perrin, M. D., Soummer, R., Elliott, E. M., Lallo, M. D., & Sivaramakrishnan, A. 2012, Proc. SPIE, 8442, 84423D
Perry, R W, Chapman, S C, Smail, Ian, & Bertoldi, F 2023, MNRAS, 523, 2818
Pillepich, A., Nelson, D., Springel, V., et al. 2019, MNRAS, 490, 3196
Planck Collaboration, Aghanim, N., Akrami, Y., et al. 2020, A&A, 641, A6
Refregier, A. 2003, MNRAS, 338, 35
Refregier, A., & Bacon, D. 2003, MNRAS, 338, 48
Rieke, M. J., Kelly, D. M., Misselt, K., et al. 2023, PASP, 135, 028001
Reuter, C., Vieira, J. D., Spilker, J. S., et al. 2020, ApJ, 902, 78
Rizzo, F., Vegetti, S., Fraternali, F., Stacey, H. R., & Powell, D. 2021, MNRAS, 507, 3952
Rizzo, F., Vegetti, S., Powell, D., et al. 2020, Natur, 584, 201
Robertson, B., Bullock, J. S., Cox, T. J., et al. 2006, ApJ, 645, 986
Rybak, M., Hodge, J. A., Vegetti, S., et al. 2020, MNRAS, 494, 5542
Sanders, D. B., Soifer, B. T., Elias, J. H., et al. 1988, ApJ, 325, 74
Sotillo-Ramos, D., Pillepich, A., Donnari, M., et al. 2022, MNRAS, 516, 5404
Speagle, J. S., Steinhardt, C. L., Capak, P. L., & Silverman, J. D. 2014, ApJS, 214, 15
Spilker, J. S., Aravena, M., Phadke, K. A., et al. 2020, ApJ, 905, 86
Spilker, J. S., Marrone, D. P., Aravena, M., et al. 2016, ApJ, 826, 112
Steinmetz, M., & Navarro, J. F. 2002, NewA, 7, 155
The CASA Team, Bean, B., Bhatnagar, S., et al. 2022, PASP, 134, 114501
Vieira, J. D., Marrone, D. P., Chapman, S. C., et al. 2013, Natur, 495, 344
Wright, Gillian S., Rieke, George H., Glasse, Alistair, et al. 2023, PASP, 135, 048003